RSC Advances

PAPER

View Article Online
View Journal | View Issue

Cite this: *RSC Adv.*, 2019, **9**, 36020

Effect of Cu^{2+} on the nucleation kinetics and crystallization of rod-shaped $CaSO_4 \cdot 2H_2O$ in aqueous solution†

Xiangbin Sun,[a] Xianshun Wang,[a] Genlei Zhang,*[abc] Peng Cui*[a] and Hao Shen[c]

Received 20th September 2019
Accepted 29th October 2019

DOI: 10.1039/c9ra07640a

rsc.li/rsc-advances

In this study, a simple and efficient strategy is developed to synthesize rod-like $CaSO_4 \cdot 2H_2O$ (DH) crystals with tunable aspect ratio in aqueous solution using Cu^{2+} as modifier. The aspect ratio and length of the DH crystals are effectively reduced to 5.7 : 1 and about 35 μm in the presence of Cu^{2+}, respectively. The interfacial tension value (γ) in the aqueous solution is improved significantly with the assistance of Cu^{2+}, yet the nucleation rate (J) of the DH crystal is decreased sharply. The interfacial tension value (γ) in the aqueous solution is improved and the nucleation rate (J) of the DH crystal is drastically decreased due to the introduction of Cu^{2+}, leading to the induction time of the DH crystallization being extended from 4 min to 25 min. The diversification of morphology for the DH crystals is incited by the changes of nucleation kinetics and Cu^{2+} incorporated into the crystal lattice, affecting the crystal growth habit, and finally controlling the growth of DH crystals in aqueous solution.

1. Introduction

Calcium sulfate is a common inorganic compound which is of huge environmental and industrial importance. In nature, it is present as large-scale deposits of $CaSO_4 \cdot 2H_2O$ (DH), $CaSO_4 \cdot 0.5H_2O$ (HH) and $CaSO_4$ (AH),[1–4] and is the source material for the preparation of high volumes of compounds including plaster and cement and for use in agricultural applications.[5–7] In particular, DH, as a crucial mineral, is widely used in industry for bone tissue regeneration, as a medical carrier and in 3D-printing.[8–11] However, in addition to these highly profitable applications, undesirable DH precipitation can also induce huge damage in industrial processes that depend on water handling systems such as waste water treatment, desalination plants and oil/gas production, where the accumulation of its precipitates can seriously impede flow and reduce production efficiency.[12–14] The size, morphology and nucleation rate of DH crystals are closely related, it is thus not surprising that a plethora of studies focused on elucidating the nucleation and growth mechanism of DH.[15–20]

Controlling the crystallization induction time (t_{ind}) and crystal morphology of the DH crystal can be achieved by changing the crystallization chemistry of the system. The most effective and widely used strategy is the introduction of soluble additives, where these can effectively affect nucleation period and growth processes, and resulting in variation for particle phases, sizes as well as morphology. Numerous investigations on the inorganic and organic additives affect the crystallization have been well documented.[21–26] Organic acids and carboxyl-rich polymers such as fulvic acid (FA),[27] sodium dodecyl sulfonate (SDS),[28,29] and polyacrylic acid (PAA)[30] have been shown to be particularly effective in inhibiting induction period for crystallization. The mechanism of action of organic additives is mainly to complex the active groups of organic substances or to adsorb Ca^{2+} in aqueous solution, reduce the supersaturation of the system to prolong the induction time of DH crystals, and form a shell-like structure on the surface of the crystal. The directional migration of Ca^{2+} is hindered in aqueous solution. Thus, the DH crystal growth suppressed and formed a smaller size.

The crystallization time of the DH crystal in the aqueous phase can be significantly extended in the presence of inorganic ions such as K^+, Na^+, Li^+ and Mg^{2+}.[31,32] K^+ and Na^+ have little effect on the DH product, and the DH crystal size and morphology are basically unchanged. However, Li^+ and Mg^{2+} can double the length of the DH crystal, but the crystal width changes slightly compared to the blank.[33] The nucleation surface energy of the DH crystal is reduced in the presence of Mg^{2+}, which leads to prolonged DH crystal induction time.[34] Mg^{2+} ionic radius is smaller than Ca^{2+}, the XRD peak of the DH crystal shifted to higher 2θ angles and the unit cell volume decreases in presence of Mg^{2+}, which suggested Mg^{2+} acts by substituting the Ca^{2+} ions in the DH crystals lattice.[35] Cu^{2+}, as a typical divalent metal cation, has been reported as an

[a]School of Chemistry and Chemical Engineering, Anhui Province Key Laboratory of Controllable Chemistry Reaction and Material Chemical Engineering, Hefei University of Technology, Hefei 230009, China. E-mail: genleizhang@hfut.edu.cn; cuipeng@hfut.edu.cn

[b]School of Materials Science and Engineering, Hefei University of Technology, Hefei 230009, China

[c]Anhui Liuguo Chemical Co. Ltd, Tongling 244021, China

† Electronic supplementary information (ESI) available. See DOI: 10.1039/c9ra07640a

inorganic additive for the regulation of HH morphology.[31] However, there is few reports on the Cu^{2+} used as an inorganic additive for the regulation of DH morphology and its effect in the crystallization process has not been revealed clearly.

In this study, we developed a simple strategy for the synthesis of controllable aspect ratio rod-shaped DH crystals, and Cu^{2+} is widely significance in controlling the morphology of DH crystals. The influence of dynamic parameters such as interfacial tension values and nucleation rates were investigated, the diversification of morphology for the crystallization of DH crystals is incited by the changes of nucleation kinetics and Cu^{2+} incorporated into the crystal lattice, affecting the crystal growth habit in aqueous solution.

2. Experimental

2.1 Experimental procedure

Analytical grade chemicals used and purchased from the Sinopharm Chemical Reagent Co. Ltd. (Shanghai, China) in this nucleation experiment. All crystallization tests were executed in a 500 dm^3 thermostatic double-walled glass vessel equipped with a Teflon stirrer, a cooled condenser and a Thermocouple. The constant temperature of the reactor was stably controlled by the oil bath circulation between the double walls and oil bath. 100 dm^3 of $CaCl_2$ solution and $CuCl_2$ (0–20 mM) mixed with deionized water was preheated to working temperature (70 °C) in the reactor, and stirring constantly at 100 rpm. Equal volume (100 dm^3) of equimolar Na_2SO_4 was also preheated to the same experimental temperature (70 °C), and quickly mixing it into the reactor. Once mixed, solution was supersaturated, and as the experiment progresses DH will be produced. At the end of each test, the slurry was hot-filtered by a 0.45 μm cellulose membrane, and the sample was washed three times with boiling water and rinsed with ethanol then dried for 2 h at 45 °C in a vacuum drying oven before further analyses.

The effect of Cu^{2+} on DH solubility were evaluated by adding $CuCl_2$ (0–20 mM) to supersaturated DH slurry, and stirred at 70 °C for 48 hours. 1 mL of solution was filtered by a syringe filter with a 0.45 μm cellulose membrane and quickly diluted with deionized water in a 100 mL of volumetric flask for measure the concentration of Ca^{2+}. Each experimental set was executed three times to ensure the accuracy of the data.

2.2 Characterization

The Atomic Absorption Spectroscopy (AAS) used in this study to determine total Ca^{2+} concentration in the filtrate by AA-6300C AAS instrument (Shimadzu; Japan). Induction time of the DH crystals were monitored by measure the ionic conductivity using a LE703 conductivity meter (METTLER TOLEDO; Switzerland). The scanning electronic microscopy (SEM) images of DH crystals were investigated using a SU8020 scanning electron microscope (Hitachi; Japan) with an accelerating voltage of 10 kV. The transmission electron microscopy (TEM) and high-resolution TEM (HRTEM) equipped with selected area electron diffraction (SAED) were performed using JEOL 2100F microscope (JEOL; Japan) operated at 200 kV. The energy dispersive X-ray spectroscopy (EDS) analysis was conducted using the TEM to examine the chemical composition of samples. The crystallographic characteristics of the DH crystals were investigated utilizing powder X-ray diffraction (XRD) using a D/max-γB X-ray diffractometer (Rigaku; Japan) with Cu K_α radiation ($\lambda = 0.15406$ nm) operated at 40 kV and 80 mA. The X-ray photoelectron spectroscopy (XPS) data of DH crystals were recorded using a ESCALAB250Xi X-ray photoelectron spectrometer (Thermo Scientific; USA) with using a monochromatized Al Kα ($h = 1486.6$ eV) X-ray source.

2.3 Experimental procedure

The interfacial tension gap the supersaturated aqueous and the crystals (γ, J m^{-2}) is a crucial factor at the rate of nucleation and crystal growth. The interfacial tension could be estimated from the induction time of crystals as a function of supersaturation. Based on classical nucleation theory,[36] the induction procedure of DH nucleation, defined as the period time between the generation of nuclei and the initial supersaturated solution which caused changes in physical parameters. The induction time and supersaturation correlated by the following equation:[37,38]

$$\lg(t_{\text{ind}}) = A + \frac{B}{(\log S)^2} \tag{1}$$

where A is a frequency constant (dimensionless) and B is a variable. The value of B could be obtained by plotting of $\lg(t_{\text{ind}})$ against $\lg^{-2}(S)$ over a range of supersaturation ratios at 70 °C. Respectively, the relative supersaturation (S) and the interfacial tension (γ) could be calculated by eqn (2) and (3):

$$S = \frac{C}{C^*} \tag{2}$$

$$\gamma = 2.3RT\left(\frac{B}{\beta V_{\text{m}}^2 N_{\text{A}} f(\theta)}\right)^{\frac{1}{3}} \tag{3}$$

where R is the gas constant (J mol^{-1} K^{-1}) and T is the absolute temperature (K). β is a geometric factor, the value of $16\pi/3$ for a spherical nucleus and 32 for a cube. V_{m} is the molar volume (74.69 cm^3 mol^{-1} for DH), N_{A} is Avogadro's number (mol^{-1}) and $f(\theta)$ is a correction factor for heterogeneous nucleation. When purely homogeneous nucleation occurs, the value of $f(\theta)$ is 1 and when heterogeneous nucleation takes place it is 0.01. It has been reported that the change in the slope of B may imply a transformation of nucleation mechanism from homogeneous to heterogeneous nucleation.[39]

The nucleation rate (J) defined as the number of nucleation per unit time per unit volume (nuclei per m^3 per s), can be calculated from the following equation:

$$J = F\exp\left[\frac{-\beta\gamma^3 V_{\text{m}}^2 N_{\text{A}} f(\theta)}{(RT)^3 In^2 S}\right] \tag{4}$$

where F is a frequency constant and named as the pre-exponential factor, the theoretical value is 10^{30} nuclei per cm^3 per s.[34]

3. Results and discussion

The scanning electronic microscopy (SEM) images of end-product crystals prepared with the aid of 20 mM Cu^{2+} in aqueous solution is shown in Fig. 1a, which exhibits the obtained crystal in the morphology of the long rod having an average length of 35 ± 5 μm (which is shown in Fig. 2d) and an average aspect ratio of about 5.7 : 1 (Fig. S1†). The X-ray diffraction (XRD) pattern of the obtained crystals is shown in Fig. 1b and the main diffraction peaks about at 11.67°, 20.79°, 23.42°, 29.16° and 31.20° are assigned to $CaSO_4 \cdot 2H_2O$ (020), (021), (040), (041) and (−221) facets (JCPDS 33-0311),[40] respectively.

XRD result shows that the rod-like crystals obtained is $CaSO_4 \cdot 2H_2O$ in the presence of 20 mM Cu^{2+} and are noted as DH-20 in this work.

Transmission electron microscopic (TEM), selected area electron diffraction (SAED), high resolution electron microscopy (HRTEM) and energy dispersive X-ray spectroscopy (EDS) have been performed to investigate the morphology and structure of DH-20 further. The TEM image (Fig. 1c) shows that circular edge apparent in the top of the DH-20 crystal, and the indexes of the spots in the SAED pattern (Fig. 1d) corresponding to the orange square region in Fig. 1c indicate that the DH-20 crystal is single-crystalline.[41] The fringe spacing of 0.63 nm in the HRTEM image (Fig. 1e) corresponds to the (020) plane, indicating the preferential growth of the DH-20 along the (020) direction.[17,19] Ca, S and O elements are homogeneously distributed throughout the while DH-20 crystal, which is confirmed by EDS elemental mapping images (Fig. 1f–h). Besides, Cu signal is also detected and its distribution is similar to the above three elements (Fig. 1i). The Cu signal detected in the obtained DH-20 indicates that Cu^{2+} may be adsorbed on the surface or doped into the lattice of DH.

In order to study the effect of Cu^{2+} on the morphology of DH, series of concentration-dependent experiments were conducted, and DH-0, DH-2 and DH-5 were prepared assisting by 0 mM, 2 mM and 5 mM Cu^{2+}, respectively. The above three samples were characterized by SEM shown in Fig. 2a–c, and the average length, width and aspect ratio were displayed in Fig. 2d and S1†, respectively. As combining indicated by Fig. 1a and 2a–c, the long rod shape of DH is hardly affected by Cu^{2+} besides the length, width and aspect ratio. The length, width and aspect ratio of DH crystals were depended on the concentration of Cu^{2+}, as displayed in Fig. 2d and S1†, when the concentrations of Cu^{2+} were 0 mM, 2 mM, 5 mM and 20 mM, respectively, the average aspect ratios were 9.7/1, 9.4/1, 8.3/1 and 5.7/1, and the average lengths were about 197 μm, 153 μm, 82 μm and 35 μm in turn. According to the theoretical fundamentals of crystal growth, the final external shape of a crystal depends on the relative growth rates of different crystal faces, which could be controlled by modifying the thermodynamic or kinetic parameters of the crystallization environment.[17,42] In this study, the addition of Cu^{2+} significantly inhibits the growth of the DH crystal along the length and width directions and more finely divided DH crystals with a smaller aspect ratio are formed.

The crystals noted as DH-20 is $CaSO_4 \cdot 2H_2O$ in nature, which is indicated by its XRD pattern (Fig. 1b). The XRD patterns of DH-0, DH-2 and DH-5 are presented in Fig. 3 and S2a,† and obviously, these XRD patterns are all similar to that of DH-20 (green curve in Fig. 1 and 3), which indicates the DH-0, DH-2 and DH-5 synthesized are all $CaSO_4 \cdot 2H_2O$ crystals in the aqueous solution in the absence (black curve in Fig. 3) or presence (red, purple and green curves in Fig. 3) of Cu^{2+}. In addition, it is noted that the (020) peak shifts to larger angles with increasing the Cu^{2+} concentration (Fig. 3), as well as the other XRD peaks (Fig. S2b†). The above phenomenon indicates that Cu atoms have been successfully incorporated into the

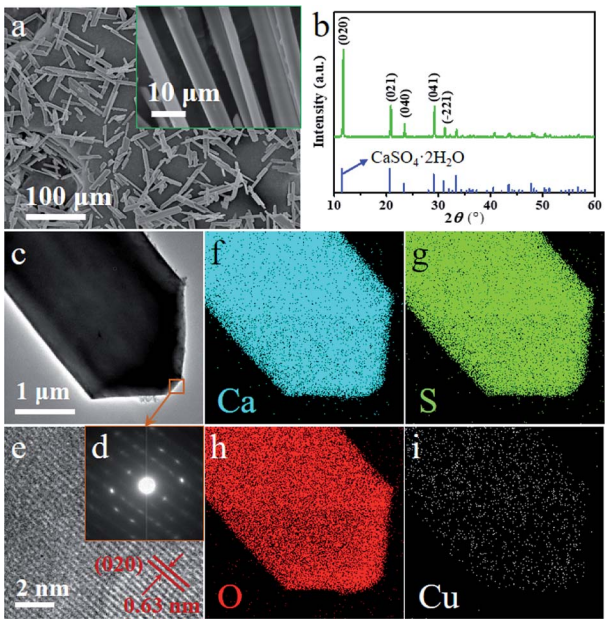

Fig. 1 (a) SEM images, (b) XRD pattern, (c) TEM and (d) SAED pattern from the orange square region in (c); (e) HRTEM images of the DH-20 crystals prepared with the aid of 20 mM Cu^{2+} in aqueous solution and (f–i) EDS element mapping images corresponding to (c).

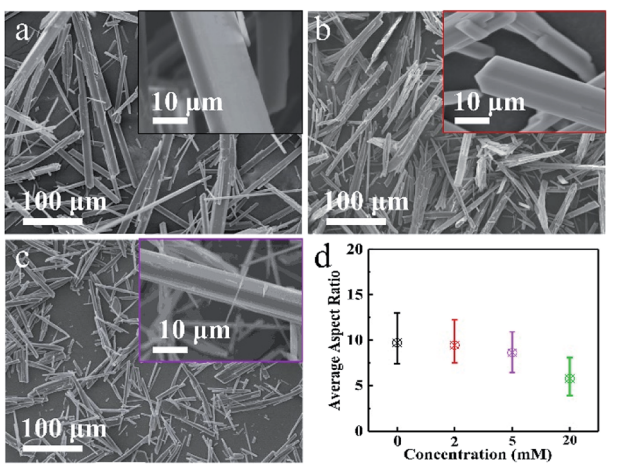

Fig. 2 SEM images of (a) DH-0, (b) DH-2 and (c) DH-5 crystals prepared assisted by 0 mM, 2 mM and 5 mM Cu^{2+}, respectively; (d) average aspect ratios of DH-0, DH-2, DH-5 and DH-20.

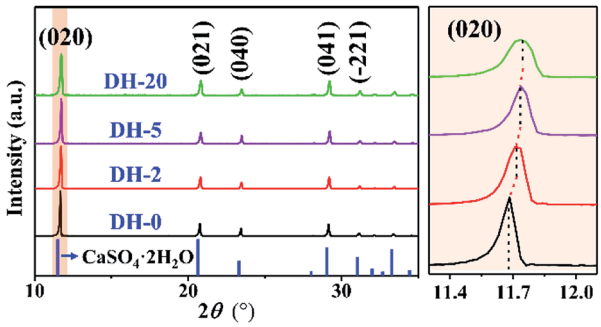

Fig. 3 XRD patterns of DH-0, DH-2, DH-5 and DH-20 crystals.

lattice of $CaSO_4 \cdot 2H_2O$.[33,35] Beyond that, the gradual decrease of peak intensity and the slight increase in the peak width with the introduction of Cu^{2+} indicates the grain size is minimal and the crystallinity is decrease after Cu is doped into $CaSO_4 \cdot 2H_2O$. This indicates that the doping of Cu into $CaSO_4 \cdot 2H_2O$ lattice inhibit crystal growth, agreeing with the results of the length and width (Fig. S1†). The unit cell parameters calculated from XRD patterns of DH crystals listed in Table 1. With the addition of Cu^{2+}, the value of *a* for the unit cell is increased and the unit cell volume is expanded, although the value of *c* is reduced. The data from the Table 1 indicate that the unit cell of DH is distorted when Cu^{2+} is added during DH crystallization.

The influence behavior of Cu^{2+} on the obtained DH crystals was also illustrated by X-ray photoelectron spectroscopy (XPS), and all of the binding energies (BEs) were calibrated using C 1s as the reference energy at 284.5 eV. Fig. 4a and b show the XPS spectra of the S 2p and Cu LMM regions of DH-0 prepared without $CuCl_2$, respectively. For comparison, the XPS spectra of the S 2p and Cu LMM regions for DH-2, DH-5 and DH-20 are also shown in Fig. 4a and b, respectively. Compared to the S $2p_{1/2}$ spectrum of DH-0, an obvious negative shift (about 0.2 eV) in the binding energy was observed for DH-2, DH-5 and DH-20 (Fig. 4a), and the specific values of the XPS peak positions are listed in Table 2. The Cu signal is observed in DH-2, DH-5 and DH-20 except DH-0 (Fig. 4b), indicating that Cu element is doped into the DH crystal when $CuCl_2$ is present in the reaction system. The shifts in the BE for S $2p_{1/2}$ and the appearance of the Cu signal in Cu LLM indicate an interaction between SO_4^{2-} and Cu^{2+} in DH-2, DH-5 and DH-20.[43] The above evidence indicates speculate the possible Cu^{2+} doping into the lattice gap of the DH unit cell structure and affecting the crystal growth

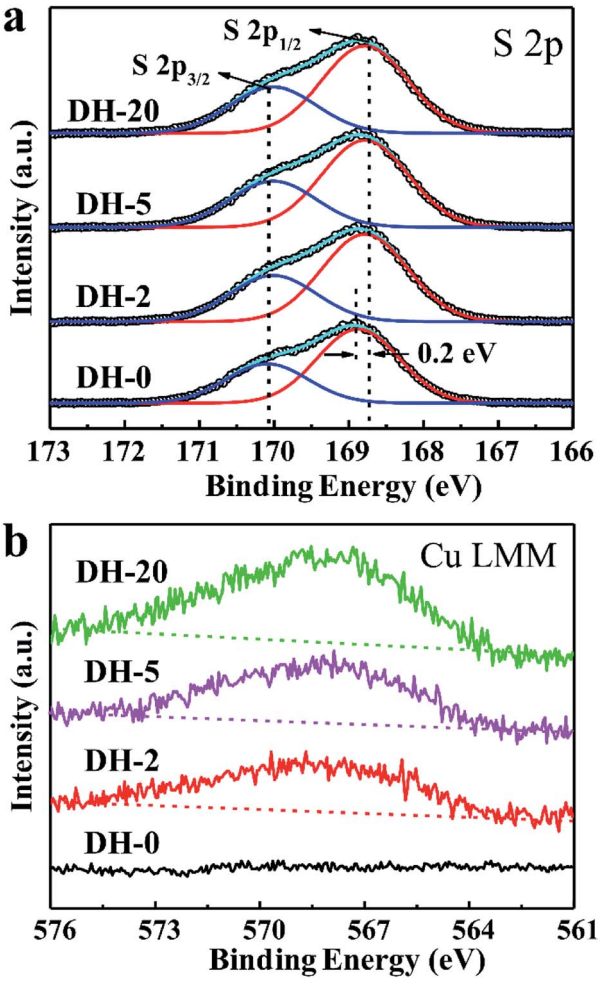

Fig. 4 (a) S 2p and (b) Cu LLM XPS spectra of DH-0, DH-2, DH-5 and DH-20 crystals prepared with the aid of $CuCl_2$ with different concentration.

habit which leaded the controlling the crystal morphology in aqueous solution ultimately.

The nucleation and growth rates of the DH crystal are determined by its equilibrium solubility (C^*), and according to several previous reports,[44–47] the value of C^* in this system can be measured by a seeded growth equilibration method and the data are displayed in Table 3. The C^* value of saturated gypsum solution can be increased effectively by the introduction of Cu^{2+}, and as the concentration of Cu^{2+} increases, the C^* value is

Table 1 The cell parameters calculated from XRD patterns of DH crystals which prepared by $CuCl_2$ aqueous solution with different concentration

Cu^{2+} concentration (mM)	*a* (Å)	*b* (Å)	*c* (Å)	*β* (deg)	*V* (Å^3)
0	6.1965	15.2443	5.7300	114.2731	493.4027
2	6.2351	15.2221	5.7295	114.4721	494.9321
5	6.2406	15.2537	5.7218	114.3853	496.0781
20	6.2586	15.2496	5.7182	114.1812	497.8629

Table 2 S 2p and Cu LLM XPS peaks values of DH-0, DH-2, DH-5 and DH-20 crystals

Sample	S $2p_{1/2}$ (eV)	S $2p_{3/2}$ (eV)	Cu LMM (eV)
DH-0	168.9	170.1	—
DH-2	168.7	170.1	568.1
DH-5	168.7	170.1	568.1
DH-20	168.7	170.1	568.1

Table 3 The solubility (C^*) of DH in aqueous solution solutions with different Cu^{2+} concentration at 70 °C

Cu^{2+} concentration (mM)	C^* (mM)
0	14.31
2	14.56
5	15.13
20	17.42

Table 4 Estimated γ values and nucleation rates (J) of DH in aqueous solution with different Cu^{2+} concentration at 70 °C

Cu^{2+} concentration (mM)	γ (mJ m^{-2})	J ($\times 10^{28}$ nuclei per cm^3 per s)
0	6.32	60.11
2	8.07	34.65
5	8.75	25.90
20	9.46	18.14

increased gradually. The above data in Table 3 provides evidence for the calculation of the relative supersaturation (S) and the interfacial tension (γ) during the subsequent DH crystallization.

The effect of concentration of Cu^{2+} on the DH crystallization is shown in Fig. 5a. Induction time (t_{ind}) is defined as the time required for the commencement of crystallization or it is the time elapsed until the moment at which the onset of crystallization can be detected. The commencement of crystallization in our experiments was detected by drop in conductivity. When the conductivity decreases rapidly, crystallization is visible. It is apparent from Fig. 5a that the t_{ind} increases with the increase in concentration of Cu^{2+}. The t_{ind} is extended from 4 min to 11 min, 15 min and 25 min when the concentration of Cu^{2+} are 2 mM, 5 mM and 20 mM, respectively. Later on the crystal growth recommences with a measurable rate observed by a drop in conductivity. The linear change of conductivity for gypsum nucleation in the presence of Cu^{2+} at 70 °C was employed to calculate the values of interfacial tension and the rate of nucleation process. The effect of increasing the supersaturation on reducing the induction period was showed in Fig. 5b. The straight lines with different slopes suggest that two nucleation mechanisms may exist for DH crystallization. The behavior of high supersaturation crystallization is more consistent with a homogeneous nucleation mechanism (region I) in contrast to lower supersaturation where heterogeneous nucleation mechanism (region II) is more likely. The slope of the induction period plot is used to distinguish between nucleation mechanisms,[48–51] and the relatively gentle slope is used to calculate the values of γ (listed in Table 4) according eqn (3).

As shown in Table 4, in the presence of Cu^{2+}, the γ is preceded by an induction time of several minutes to several thousand minutes. Obviously, the γ increases sharply in the presence of Cu^{2+} (8.07 mJ m^{-2} for 2 mM Cu^{2+} *vs.* 6.32 mJ m^{-2} for 0 mM Cu^{2+}), and the γ increases slowly as the Cu^{2+} concentration continues to increase. The γ value of 9.46 mJ m^{-2} was obtained when the Cu^{2+} concentration is 20 mM, corresponding to a significant increase of about 49% with respect to the γ value for the additive-free series. Higher nucleation energy needs to be overcome to form a critical nucleus in a nucleation process when the γ value is large, which reflects extension of the t_{ind} for crystallization period in the presence of Cu^{2+}. Theoretically, controlling the crystal morphology and diameter is closely related to the nucleation rates.[52–54] The rate of spherical DH nucleation can be estimated from eqn (4), and the date are listed in Table 4. The nucleation rate of DH would be decreased due to the introduction of Cu^{2+}, and when the of Cu^{2+} concentration is increased to 20 mM, the corresponding nucleation rate is reduced to 1/3 of that in the absence of Cu^{2+} (18.14×10^{28} nuclei per cm^3 per s *vs.* 60.11×10^{28} nuclei per cm^3 per s). The data of EDS (Fig. 1), XRD (Fig. 3) and XPS (Fig. 4) indicate that the Cu^{2+} doping into the crystal lattice, similar to other metal cations (such as Mg^{2+} and Al^{3+}) on the morphology of DH,[35,55] thereby controlling DH crystallization rate and crystal size. Therefore, the nucleation rate of DH can be effectively inhibited by Cu^{2+}, which results in a significant change in crystal morphology and size.

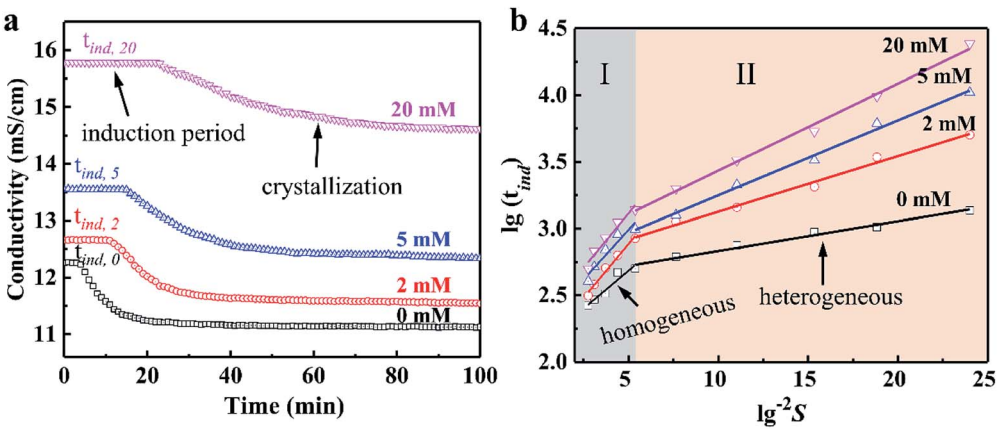

Fig. 5 (a) Crystallization behavior of a supersaturated solution of DH (b) the homogeneous-heterogeneous nucleation transition by plotting $\lg(t_{ind})$ *vs.* $\lg^{-2}(S)$ for DH crystallization at 70 °C in the absence and presence of various concentrations of Cu^{2+}.

4. Conclusions

In summary, we have developed a simple strategy for the synthesis of controllable aspect ratio rod-shaped DH crystals, and Cu^{2+} is widely significance in controlling the morphology of DH crystals. With the concentration of Cu^{2+} increased from 0 mM to 20 mM, the average aspect ratios decreased sharply from 9.7/1 to 5.7/1, and the corresponding average lengths decreased from about 197 μm to 35 μm. The nucleation kinetic parameters of the DH crystals crystallization that act as critical roles in controlling DH nucleation rate and induction time have been modified in the presence of Cu^{2+}. The induction time of the DH crystallization is extended from 4 min to 25 min using Cu^{2+} as a modifier. The diversification of morphology for the crystallization of DH crystals is incited by the changes of nucleation kinetics and Cu^{2+} incorporated into the crystal lattice, affecting the crystal growth habit in aqueous solution.

Conflicts of interest

There are no conflicts to declare.

Acknowledgements

This work is financially supported by Natural Science Foundation of China (21806065) and Doctoral Special Research Foundation of HFUT (JZ2018HGBZ0122 and JZ2018HGBZ0087). We also thank the support from Anhui Province Key Laboratory of Advanced Catalytic Materials and Reaction Engineering (45000-411104/007).

References

1 D. R. Govender, W. W. Focke, S. M. Tichapondwa and W. E. Cloete, *ACS Appl. Mater. Interfaces*, 2018, **10**, 20679–20687.
2 G. Sirokman, *J. Chem. Educ.*, 2014, **91**, 557–559.
3 T. Tyner and J. Francis, *ACS Reagent Chemicals: Specifications and Procedures for Reagents and Standard-Grade Reference Materials*, ACS Publications, 2016.
4 H. Tan, F. Dong and J. Liu, *J. Phys. Chem. Solids*, 2018, **112**, 239–245.
5 D. C. Engbrecht and D. A. Hirschfeld, *Thermochim. Acta*, 2016, **639**, 173–185.
6 I. Koh, A. López, B. Helgason and S. J. Ferguson, *J. Mech. Behav. Biomed. Mater.*, 2014, **34**, 187–198.
7 N. Jiang, D. Cai, L. He, N. Zhong, H. Wen, X. Zhang and Z. Wu, *ACS Sustainable Chem. Eng.*, 2015, **3**, 374–380.
8 J. Baek, H. Lee, T. S. Jang, J. Song, H. E. Kim and H. D. Jung, *ACS Biomater. Sci. Eng.*, 2018, **4**, 846–856.
9 Z. Zhou, F. Buchanan, C. Mitchell and N. Dunne, *Mater. Sci. Eng., C*, 2014, **38**, 1–10.
10 S. Grudén, M. Sandelin, V. Rasanen, P. Micke, M. Hedeland, N. Axén and M. Jeansson, *Eur. J. Pharm. Biopharm.*, 2017, **114**, 186–193.
11 Y. Shen, S. Yang, J. Liu, H. Xu, Z. Shi, Z. Lin, X. Ying, P. Guo, T. Lin and S. Yan, *ACS Appl. Mater. Interfaces*, 2014, **6**, 12177–12188.
12 W.-Y. Shih, A. Rahardianto, R.-W. Lee and Y. Cohen, *J. Membr. Sci.*, 2005, **252**, 253–263.
13 T. A. Hoang, M. Ang and A. L. Rohl, *Chem. Eng. Technol.*, 2011, **34**, 1003–1009.
14 A. E. S. V. Driessche, J. M. GarcíA-Ruiz, J. M. Delgado-LóPez and G. Sazaki, *Cryst. Growth Des.*, 2010, **10**, 3909–3916.
15 E. H. Byrne, P. Raiteri and J. D. Gale, *J. Phys. Chem. C*, 2017, **121**, 25956–25966.
16 T. M. Stawski, A. D. Van, M. Ossorio, R. B. Diego, R. Besselink and L. G. Benning, *Nat. Commun.*, 2016, **7**, 1–19.
17 T. M. Stawski, H. M. Freeman, A. E. S. Van Driessche, J. Hövelmann, R. Besselink, R. Wirth and L. G. Benning, *Cryst. Growth Des.*, 2019, **19**, 3714–3721.
18 K. Gupta, S. Singh and M. R. Rao, *Cryst. Growth Des.*, 2016, **16**, 3256–3261.
19 S. Leukel, M. Panthöfer, M. Mondeshki, W. Schärtl, S. Plana-Ruiz and W. Tremel, *Langmuir*, 2018, **34**, 7096–7105.
20 E. R. Ravenhill, P. M. Kirkman and P. R. Unwin, *Cryst. Growth Des.*, 2016, **16**, 5887–5895.
21 X. Mu, G. Zhu, X. Li, S. Li, X. Gong, H. Li and G. Sun, *ACS Omega*, 2019, **4**, 12702–12710.
22 H. Wang, G. Liu, J. Huang, Y. Zhou, Q. Yao, S. Ma, C. Ke, Y. Liu, W. Wu and S. Wei, *Desalin. Water Treat.*, 2015, **53**, 8–14.
23 C. Fan and R. M. Pashley, *Chem. Eng. Sci.*, 2016, **142**, 23–31.
24 H. Wang, Y. Zhou, Q. Yao and W. Sun, *Polym. Bull.*, 2015, **72**, 2171–2188.
25 M. G. Lioliou, C. A. Paraskeva, P. G. Koutsoukos and A. C. Payatakes, *J. Colloid Interface Sci.*, 2006, **303**, 164–170.
26 L. Shen, H. Sippola, X. Li, D. Lindberg and P. Taskinen, *J. Chem. Eng. Data*, 2019, **64**, 2697–2709.
27 Y. Xu, Y. Liao, Z. Lin, J. Lin, Q. Li, J. Lin and Z. Jin, *Chem. Eng. J.*, 2019, **361**, 1078–1088.
28 X. Mao, X. Song, G. Lu, Y. Xu, Y. Sun and J. Yu, *Chem. Eng. J.*, 2015, **278**, 320–327.
29 X. Mao, X. Song, G. Lu, Y. Sun, Y. Xu and J. Yu, *Ind. Eng. Chem. Res.*, 2015, **54**, 4781–4787.
30 T. Rabizadeh, D. J. Morgan, C. L. Peacock and L. G. Benning, *Ind. Eng. Chem. Res.*, 2019, **58**, 1561–1569.
31 G. Jiang, H. Fu, K. Savino, J. Qian, Z. Wu and B. Guan, *Cryst. Growth Des.*, 2013, **13**, 5128–5134.
32 T. Feldmann and G. P. Demopoulos, *Ind. Eng. Chem. Res.*, 2013, **52**, 6540–6549.
33 T. Rabizadeh, T. M. Stawski, D. J. Morgan, C. L. Peacock and L. G. Benning, *Cryst. Growth Des.*, 2017, **17**, 582–589.
34 M. M. Rashad, M. H. H. Mahmoud, I. A. Ibrahim and E. A. Abdel-Aal, *J. Cryst. Growth*, 2004, **267**, 372–379.
35 S. B. Ahmed, M. M. Tlili, M. Amami and M. B. Amor, *Ind. Eng. Chem. Res.*, 2014, **53**, 9554–9560.
36 J. C. Brice and P. Rudolph, *Ullmann's Encyclopedia of Industrial Chemistry*, 2000.
37 M. Prisciandaro, A. Lancia and D. Musmarra, *Ind. Eng. Chem. Res.*, 2003, **42**, 6647–6652.

38 B. Guan, L. Yang and Z. Wu, *Ind. Eng. Chem. Res.*, 2010, **49**, 5569–5574.
39 F. Wang, T. E. Davis and V. V. Tarabara, *Ind. Eng. Chem. Res.*, 2010, **49**, 11344–11350.
40 X. Sun, G. Zhang and P. Cui, *RSC Adv.*, 2019, **9**, 21601–21607.
41 T. Lehnert, M. K. Kinyanjui, A. Ladenburger, D. Rommel, K. Wörle, F. Börrnert, K. Leopold and U. Kaiser, *ACS Nano*, 2017, **11**, 7967–7973.
42 L. Zhang, L. Yu, Y. Liu, C. Liu, H. Li and J. Wu, *Mater. Sci. Eng., A*, 2017, **695**, 66–73.
43 K. Liu, J. Yang, H. Hou, S. Liang, Y. Chen, J. Wang, B. Liu, K. Xiao, J. Hu and H. Deng, *Environ. Sci. Technol.*, 2019, **53**, 2748–2757.
44 T. J. Trivedi, J. Shukla and A. Kumar, *J. Chem. Eng. Data*, 2013, **58**, 773–779.
45 J. Shukla, M. J. Mehta and A. Kumar, *J. Chem. Eng. Data*, 2019, **64**, 536–544.
46 J. Sun, L. Wang and G. Yu, *J. Chem. Eng. Data*, 2015, **60**, 2559–2566.
47 J. Shukla, M. J. Mehta and A. Kumar, *J. Chem. Eng. Data*, 2018, **63**, 2743–2752.
48 X. Liu, D. Xu, M. Ren, G. Zhang, X. Wei and J. Wang, *Cryst. Growth Des.*, 2010, **10**, 3442–3447.
49 D. Zhang, Y. Wang, S. Ma, S. Wu and H. Hao, *J. Chem. Eng. Data*, 2012, **58**, 176–182.
50 H. Fu, C. Jia, Q. Chen and G. Jiang, *J. Cryst. Growth*, 2017, **470**, 143–148.
51 M. Kobari, N. Kubota and I. Hirasawa, *CrystEngComm*, 2012, **14**, 5255–5261.
52 G. Di Profio, E. Curcio, S. Ferraro, C. Stabile and E. Drioli, *Cryst. Growth Des.*, 2009, **9**, 2179–2186.
53 E. Abdel-Aal, M. Rashad and H. El-Shall, *Cryst. Res. Technol.*, 2004, **39**, 313–321.
54 H. Fu, B. Guan, G. Jiang, M. Z. Yates and Z. Wu, *Cryst. Growth Des.*, 2012, **12**, 1388–1394.
55 W. Zhao, C. Gao, G. Zhang, J. Xu, C. Wang and Y. Wu, *New J. Chem.*, 2016, **40**, 3104–3108.